Prepared for submission to JINST

Investigation of Electron Backscattering on Silicon Drift Detectors for the Sterile Neutrino Search with TRISTAN

D. Spreng ,[a,b,1] **K. Urban,**[a,b] **M. Carminati,**[c,d] **F. Edzards,**[a,b] **C. Fiorini,**[c,d] **P. Lechner,**[e] **A. Nava,**[c,f] **D. Siegmann,**[a,b] **C. Wiesinger,**[a,b] **and S. Mertens**[a,b]

[a] *Technical University of Munich, TUM School of Natural Sciences, Physics Department, James-Franck-Str. 1, 85748 Garching, Germany*

[b] *Max Planck Institute for Physics, Boltzmannstr. 8, 85748 Garching, Germany*

[c] *INFN, Sezione di Milano, Via Celoria 16, 20133 Milano, Italy*

[d] *DEIB, Politecnico di Milano, Via Golgi 40, 20133 Milano, Italy*

[e] *Halbleiterlabor der Max-Planck-Gesellschaft, Isarauenweg 1, 85748 Garching, Germany*

[f] *Universita degli Studi di Milano-Bicocca, Piazza dell'Ateneo Nuovo, 1-20126, Milano, Italy*

E-mail: daniela.spreng@tum.de

Abstract: Sterile neutrinos are hypothetical particles in the minimal extension of the Standard Model of Particle Physics. They could be viable dark matter candidates if they have a mass in the keV range. The Karlsruhe tritium neutrino (KATRIN) experiment, extended with a silicon drift detector focal plane array (TRISTAN), has the potential to search for keV-scale sterile neutrinos by measuring the kinematics of the tritium β-decay. The collaboration targets a sensitivity of 10^{-6} on the mixing amplitude $\sin^2\Theta$. For this challenging target, a precise understanding of the detector response is necessary. In this work, we report on the characterization of electron backscattering from the detector surface, which is one of the main effects that influence the shape of the observed energy spectrum. Measurements were performed with a tandem silicon drift detector system and a custom-designed electron source. The measured detector response and backscattering probability are in good agreement with dedicated backscattering simulations using the Geant4 simulation toolkit.

Keywords: Detector modeling and simulations I, Interaction of radiation with matter, Solid state detectors, Large detector systems for particle and astroparticle physics

[1] Corresponding author.

Contents

1 Introduction

Sterile neutrinos have gained significant attention in the field of particle physics and astrophysics. In the scope of a minimal extension to the Standard Model of Particle Physics (SM), they are postulated as the right-handed counterparts to the well-known left-handed neutrinos [1]. As a consequence, an additional new neutrino mass eigenstate is introduced. While left-handed neutrinos actively participate in weak interactions, right-handed neutrinos do not interact via any of the fundamental forces described by the SM. Right-handed neutrinos only interact via the gravitational force of the new mass eigenstate and their mixing with the active neutrino flavors. In the following, the new mass eigenstate is referred to as 'sterile neutrino'.

The introduction of sterile neutrinos addresses various unresolved questions in cosmology and neutrino physics, contingent upon factors such as their mass m_s, the mixing with the active flavor (described by the mixing amplitude $\sin^2\Theta$), and the production mechanism [1–3]. By incorporating sterile neutrinos into the framework of the SM, they offer a natural mechanism for mass generation for active neutrinos [4]. Sterile neutrinos are not constrained to a specific mass range, and those in the keV-mass scale would serve as a viable dark matter candidate [2]. As such, the mixing amplitude of sterile neutrinos has been subject to stringent constraints from indirect searches and cosmological observations of $10^{-10} < \sin^2\Theta < 10^{-6}$ in a mass range of 1 keV to 50 keV [5–10]. However, these limits are model-dependent and can be significantly relaxed by several orders of magnitude through modifications to the models of dark matter decay [11].

By analyzing the β-decay spectrum, it is possible to search for sterile neutrinos independently of cosmological and astrophysical models [12]. In a β^--decay, an electron and an electron anti-neutrino $\overline{\nu}_e$ are emitted. The measured energy spectrum of the electrons is a superposition of spectra corresponding to the different neutrino mass eigenstates which compose the neutrino flavor

eigenstate $\overline{\nu}_e$. Therefore, a keV-scale neutrino mass eigenstate would display a significantly reduced maximal electron energy compared to the other decay branches. This results in a kink-like signature at m_s below the endpoint energy E_0 of the energy spectrum, accompanied by a global distortion of the spectrum [13].

The Karlsruhe tritium neutrino (KATRIN) experiment was designed to perform high-precision measurements of the tritium β^--decay spectrum at its endpoint energy of $E_0 = 18.6\,\text{keV}$ to test the effective electron anti-neutrino mass [14]. The experiment primarily consists of a highly stable tritium source with an activity of up to 10^{11} Bq, a spectrometer section utilizing the magnetic adiabatic collimation with electrostatic (MAC-E) filter principle, and a detector section. By upgrading the detector section with a new, so-called TRISTAN detector system, the experiment will have the capability to analyze the entire energy spectrum, not just the endpoint region. The TRISTAN detector will be commissioned in the KATRIN beamline after the neutrino mass measurement campaigns are finished at the end of 2025. It will consist of modular silicon drift detector (SDD) arrays and will measure the differential energy spectrum with an energy resolution of less than 300 eV FWHM[1] at 20 keV [15]. With this upgrade, a search for sterile neutrinos with masses up to 18.6 keV and admixtures down to 10^{-6} will be possible, improving current laboratory limits by several orders of magnitude [13, 16–18].

For a sterile neutrino search with a mixing-angle sensitivity at the parts-per-million (ppm) level, a thorough understanding of the detector response is crucial. This includes all experimental influences that alter the measured spectral shape of the tritium spectrum. The detector response for SDDs is primarily dominated by electronic noise, partial charge collection at the entrance window[2] of the detector [15, 19], and the inevitable effect of electron backscattering, as illustrated in figure 1.

When an electron undergoes scattering processes inside the detector, its direction of movement randomly changes, potentially resulting in its backscattering towards the entrance window and subsequent exit from the detector. Also, secondary electrons produced in the detector by the incoming electron can escape from the detector volume. Consequently, backscattering is a major source of incomplete charge collection, affecting the measured electron spectrum over the entire energy range. The extent of backscattering depends on the initial energy E_I and incident angle θ_I of the incoming electron. Lower electron energies and higher incident angles lead to a reduced penetration depth relative to the entrance window, increasing the probability of electron escape from the detector. In addition, the presence of electric and magnetic fields in the KATRIN beamline introduces the possibility of backscattered electrons being reflected back towards the detector. Whether the backscattered electron returns to the detector, as well as the temporal and spatial difference between the first and possible second interaction with the detector, depends on the energy and the angle of the backscattered electron.

This work investigates the backscattering properties of the TRISTAN detector system at various initial electron energies and incident angles. To this end, measurements (see section 2) and GEANT4 backscattering simulations (see section 3) are performed at different electron energies and angles. By comparing the results (see section 4), we assess the ability of GEANT4 to accurately model backscattering in silicon detectors.

[1] FWHM stands for the peaks' full width at half maximum.

[2] The entrance window denotes in the scope of this work the side through which the electron enters the detector volume.

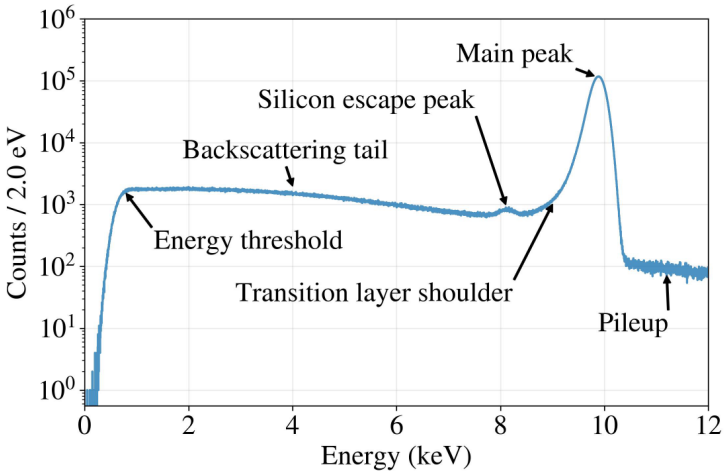

Figure 1: Measured response of the TRISTAN detector to 10 keV electrons. The detector response differs from purely Gaussian resolution effects. It is modified by various factors, including signal read-out, detector design, and physical effects. The effect of electron backscattering leads to a broad tail from the main peak down to the minimal measurable deposit energy.

2 Experimental investigations

2.1 Measurement setup

Two TRISTAN detectors are utilized to measure electron backscattering: a 7-pixel prototype detector as an active target, in the following called target detector, and a 166-pixel detector module [20] to detect the backscattered electrons, in this work called backscattering detector. The pixels are hexagons with a circumscribed diameter of approximately 3.3 mm and a thickness of 450 µm arranged in a honeycomb structure. Both detectors are mounted on copper holding structures and positioned on the cooling plate of a cylindrical vacuum chamber. Electrons from a custom-designed electron gun [21] are directed towards the target detector. The geometry of the experimental setup is depicted in figure 2.

The electron gun comprises an electrically heated tantalum wire which emits thermal electrons. A negative high voltage up to 10 kV is applied between the wire and a grounded copper electrode to accelerate these electrons. The uncertainty of the electron's kinetic energy was not measured yet, but it is expected to be in the order of 1 – 10 eV and is, therefore, negligible considering the detector energy resolution of about 200 – 300 eV in the measured electron energy range. The electrons leave the electron gun through a hole in the copper electrode. The rate of electrons reaching the target detector can be adjusted by the heating current in the wire between about 1 and 10 kcps[3].

The resulting mono-energetic electron beam is directed at the central pixel (CC) of the 7-pixel target detector. To investigate various incident angles between the electron beam and the target detector, the target detector can be rotated around the axis parallel to the center of the chip surface. The setup provides the flexibility to choose any incident angle between 0° and 60°.

[3]Here, cps abbreviates counts per second.

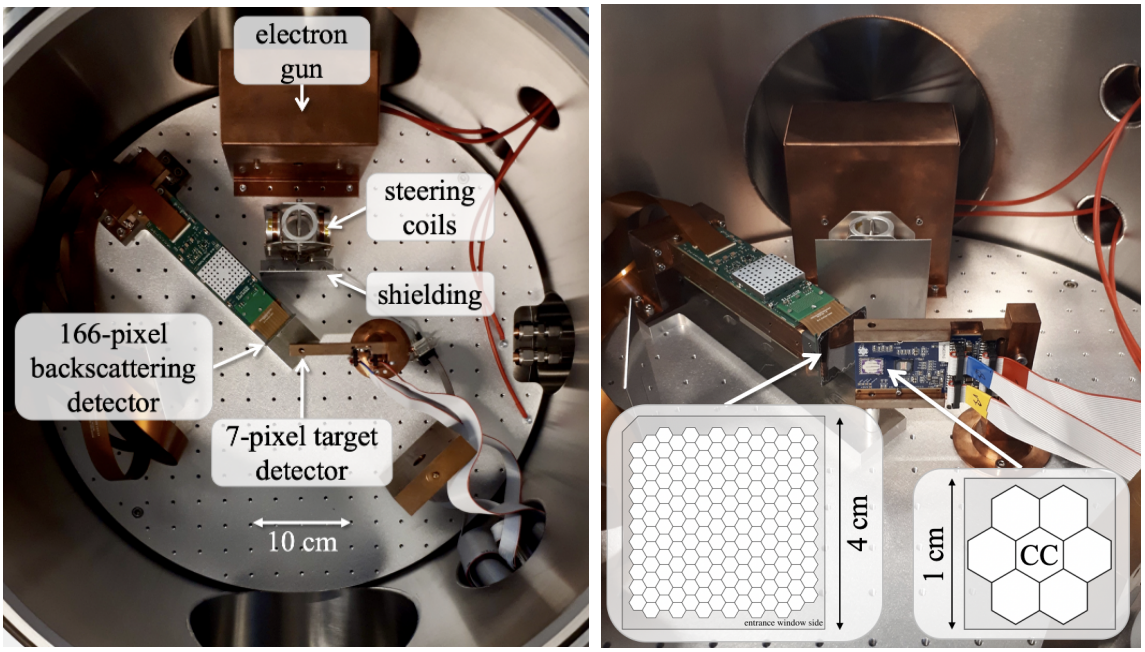

(a) Top view (b) Front view

Figure 2: In-vacuum setup. The experimental setup is depicted from a top view (figure 2a) and a front view (figure 2b). The electron gun is positioned inside a copper shielding. It emits a mono-energetic electron beam directed towards the 7-pixel target detector. The 166-pixel backscattering detector faces the target detector. Following the electron gun, steering coils and a thin plate are placed to deflect and shield misaligned electrons. The entire setup is mounted onto a cooling plate installed inside the vacuum chamber.

The 166-pixel backscattering detector faces towards the target detector to detect the backscattered electrons. Its positioning was deliberately chosen to ensure maximum angular coverage within a single measurement without a direct line of sight between the electron gun and the backscattering detector. A copper stand and an aluminum plate fixate the backscattering detector on the cooling plate flexibly. The take-off angle, representing the angle between the backscattering detector plane and the target detector plane, is set to 45°. Some pixels of the backscattering detector exhibit noisy spectra, encounter connection issues, or are partially shaded by the printed circuit board (PCB) of the target detector in the experiment. Those pixels are not considered for the later comparison of the data with the simulation.

To ensure proper alignment of the electron beam with the central pixel of the target detector, steering coils are inserted downstream from the electron gun, enabling the beam to be magnetically deflected in both horizontal and vertical directions. Furthermore, the electron beam diameter is reduced with a shielding inserted after the steering coils to safeguard the backside of the backscattering detector and the PCB of the target detector. This leads to a beam diameter of about 9 mm at the target detector plane. For the analysis, only events in the central pixel of the target detector are taken into account.

Both detectors are calibrated using an ^{55}Fe source. Afterwards, a series of nine measurements is conducted to explore different configurations of the initial energy E_I and incident angles Θ_I of the incoming electrons at the target detector. Each combination for $E_\mathrm{I} \in \{5\,\mathrm{keV}, 7.5\,\mathrm{keV}, 10\,\mathrm{keV}\}$ and $\Theta_\mathrm{I} \in \{0°, 31°, 59°\}$ is investigated. Count rates ranging from 2 to 7 kcps are observed in the central pixel of the target detector. That variation in rate occurs due to small instabilities of the electron gun and increased irradiation of the surrounding pixels at higher incident angles. For the data acquisition, three synchronized CAEN VX2740 digitizers are used. The energy, pixel number, and timestamp are recorded for every detected event in either of the detectors.

2.2 Coincidence analysis

In the experiment, all pixels of the target detector are exposed to the electron beam due to its angular spread. Since the measured backscattering properties are affected by variations in the incident angle at the target detector, it is important to extract the backscattered electrons originating only from the central pixel of the target detector. As both detectors are active, events in the backscattering detector can be correlated to events in the target detector through their timestamp. This event correlation can be accomplished with a coincidence selection. This means only events where the time difference between the event in the central pixel of the target detector and the event in the backscattering detector is shorter than a given time window are selected. In the following, a time window of 500 ns is chosen, as it is approximately the maximal electron drift time in a pixel [22]. The time the electron needs to propagate from one detector to the other is in the order of ns or below for the observed energies and the detector distances and is therefore negligible.

Figure 3 illustrates a typical energy spectrum of the incoming electrons measured by the central pixel of the target detector and the backscattered electrons measured in all pixels of the backscattering detector before and after applying the coincidence selection. In the target detector, the energy spectrum of the coincidence events mainly resembles the shape of the backscattering tail observed in the overall measured energy spectrum of the target detector. Hence, the coincidence analysis enables the identification and extraction of the signature of backscattered electrons in the target detector. The height of the backscattering tail before and after the coincidence selection differs due to the backscattering detector's incomplete angular coverage of the space.

The shape of the coincidence spectrum measured in the backscattering detector also resembles the shape of the total recorded backscattering spectrum. The fact that not all events in the backscattering detector are also coincidence events can be explained by the relative number of electrons impacting the central pixel of the target detector rather than the surrounding pixels or insensitive area.

For both detectors, the energy spectra after the coincidence selection are truncated at high energies due to the energy threshold of the detectors. If one of the events falls below the detection threshold, the other event cannot be identified as a coincidence event. This situation occurs in cases of elastic backscattering, where the initial electron is reflected at the target detector surface, or inelastic backscattering in the partially insensitive detection area at the entrance window. Additionally, secondary backscattered electrons are predominantly low-energetic and likely to fall below the backscattering detector's energy threshold. Therefore, maintaining a low energy threshold is crucial for investigating backscattering.

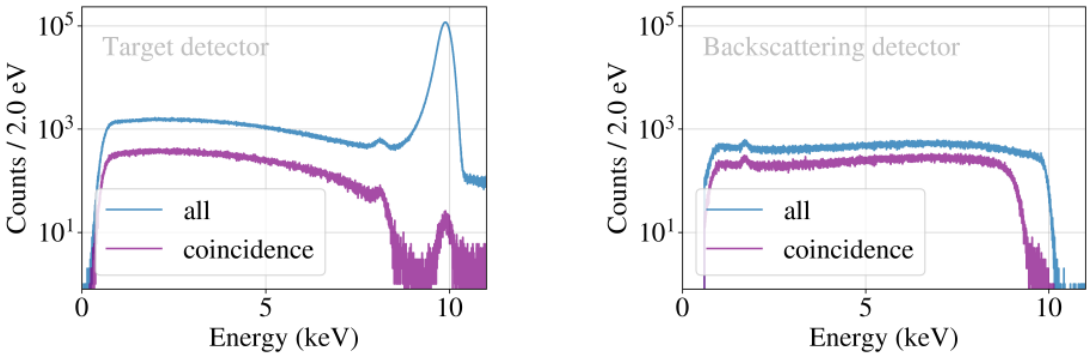

(a) Target detector

(b) Backscattering detector

Figure 3: Typical electron energy spectra with and without coincidence selection. The energy spectrum of the incoming electron measured in the central pixel of the target detector (figure 3a) and the backscattered electrons measured in any pixel of the backscattering detector (figure 3b) are shown before and after applying the coincidence cut. The spectra are shown for an initial electron energy of 10 keV and an incident angle of 0°.

The remaining electrons at high energies are caused by random coincidence; thus, an incoming and a backscattered electron just by chance simultaneously hit the detectors without causal relation. In the experiment, it is further possible for a coincidence to occur between a pileup event in the target detector and an event in the backscattering detector. To reduce both effects, an upper energy limit is imposed on the measured total energy of both coincidence events for the later comparison with the simulation. The total energy of the coincidence event in the target detector, combined with the energy of the coincidence event in the backscattering detector, must not exceed the initial electron energy, accounting for the energy resolutions of both detectors.

To keep simulation and measurements comparable, hard energy thresholds are set at higher energies. This approach is easier than modeling the actual energy threshold from the data acquisition system of the experiment. Consequently, for an event in the target detector, the corresponding event in the backscattering detector must have an energy greater than 1 keV, while for an event in the backscattering detector, the energy of the corresponding event in the target detector must not be below 0.8 keV.

3 Geant4 backscattering simulations

The experimental setup is implemented in a stand-alone application based on the GEANT4 simulation framework. The G4EMSTANDARDPHYSICSSS physics list is used for all simulations [23][4]. The difference to the default physics list for low energy physics is that it does not combine several single scattering processes into one multiple scattering process. For this reason, it is favored for backscattering investigations within this work although it is more computationally heavy. This work does not include uncertainties arising from selecting a particular GEANT4 physics list.

[4] A production cut of 100 eV is applied.

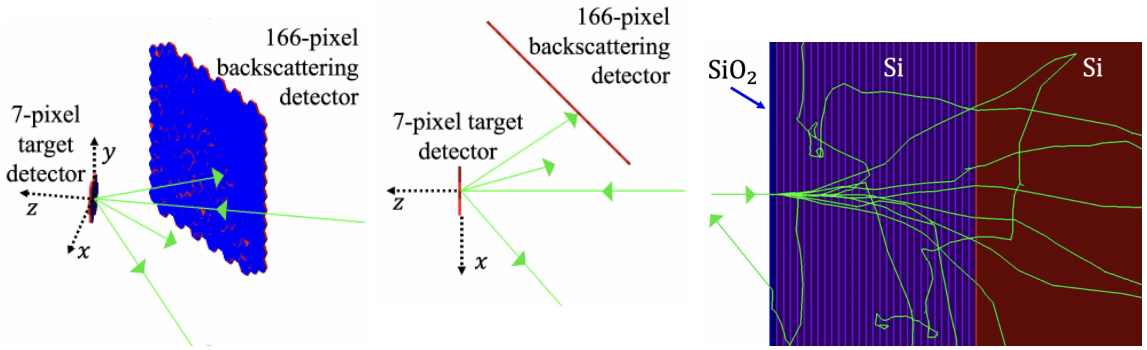

(a) Side view (b) Top view (c) Zoom on the entrance window

Figure 4: Experimental setup as implemented in the GEANT4 simulation toolkit. The setup is visualized from a side view (figure 4a) and top view (figure 4b). The arrangement of hexagon-shaped pixels, consisting of silicon (red) and a thin silicon-dioxide layer (blue), matches the experimental configuration. In figure 4c, the layers implemented to fit the charge collection efficiency at the entrance window are depicted (purple). Exemplary electron paths are displayed using green arrows, while dotted black arrows indicate the coordinate system.

In the simulation, the silicon detector pixels are generated as hexagons made of silicon with a 10 nm silicon-dioxide layer on the entrance window side[5]. The pixels are arranged in a vacuum sphere to form the 7-pixel target and the 166-pixel backscattering detector, replicating their positions within the experimental setup, see figure 4. Additional structures, such as the PCBs and copper holding structures, can be neglected in the simulation due to the coincidence analysis of the data. The read-out chain and data acquisition system are not implemented. Electronic noise and statistical fluctuations are added outside the simulation.

In the simulation, each electron is generated individually and precisely hits the central pixel of the 7-pixel target detector at its center. In this work, the actual beam profile is assumed to be negligible. The event number of each generated electron is stored to establish a correlation between the electrons detected in the 7-pixel target and 166-pixel backscattering detectors, resembling the coincidence analysis in the experiment. A total of 10 million electrons are simulated for each combination of the initial electron energy E_I and incident angle Θ_I. This is approximately in the order of measured counts in the central pixel of the 7-pixel target detector in the experiment.

For each event, the energy depositions within the pixel are summed up and recorded alongside the event and pixel number. To account for incomplete charge collection at the entrance window side, as it occurs in the experiment due to the doping profile and the resulting electric field configuration, each individual energy deposition in a pixel is weighted by the charge collection efficiency as defined in equation 3.1 [25].

$$\mathrm{CCE}(z; DL, p_1, \lambda) = \begin{cases} 0, & z < DL \\ 1 + (p_1 - 1) \cdot \exp\left(-\frac{z-DL}{\lambda}\right), & z > DL \end{cases} \tag{3.1}$$

[5]For the TRISTAN detectors, a silicon-dioxide layer is intentionally added to prevent it from growing naturally. It is manufactured with a controlled homogeneous thickness of 8 – 10 nm [15, 24].

The charge collection efficiency (CCE) of a detector pixel depends on the position z of the interaction point relative to the entrance window. The formula indicates that the detector is insensitive within a dead layer of thickness DL. Beyond this layer, the charge collection efficiency jumps to a value p_1 and then exponentially rises based on the effective transition layer thickness λ.

To determine the CCE parameters, a separate setup consisting of a single pixel is implemented in GEANT4. At the entrance window side, the pixel consists of 30 layers of 10 nm thickness each, as depicted in figure 4c. The first layer is composed of silicon-dioxide while the remaining layers and an adjoining bulk layer of 449.7 µm thickness are made of silicon. The simulation records the accumulated energy depositions for each layer and the bulk material. Simulations are performed for each E_I and Θ_I setting. The simulation is fitted to the measured data of the 7-pixel target detector with the parameters of the CCE as free parameters for each setting. The fitting process also considers possible energy miscalibrations of the detector system, electronic noise of the read-out chain in the experiment, and the difference in the number of generated incoming electrons between simulation and experiment.

The average fit results for the CCE are then incorporated into the actual backscattering simulation, assuming identical behavior for all pixels in the setup. An average dead layer thickness of $DL = 10.7^{+2.8}_{-6.7}$ nm is evaluated, which aligns with the design value of 8 – 10 nm for the thickness of the insensitive silicon-dioxide layer. The average value for p_1 is $0.856^{+0.042}_{-0.091}$. Hence, 85.6 % of the charge deposited right after the dead layer is detected. The mean effective transition layer thickness amounts to $\lambda = 75.7^{+25.1}_{-26.2}$ nm. The uncertainties here are deduced as the minimal and maximal values obtained for each parameter comparing the nine fits performed for the nine combinations of E_I and Θ_I settings.

4 Results and comparison

4.1 Electron energy spectra

In figure 5, the measured energy spectra after the coincident selection and the corresponding simulations are shown. All backscattering tails in the spectra of the central pixel of the target detector exhibit a decrease in counts as the energy depositions in the target detector increase. When examining each initial energy, the tails become steeper at lower energy depositions as the incident angle increases. In fact, for an incident angle of $\Theta_\mathrm{I} = 59°$, the decrease in counts towards higher energies in the target detector is approximately exponential until the threshold effects start to dominate the shape of the spectrum. Similar trends, albeit less pronounced, can be observed when reducing the initial energy at a fixed incident angle. Consequently, for high incident angles and low initial energies, the energy deposition in the target detector is diminished, leading to higher energy values for the backscattered electrons.

For the measurement at 0°, the shape of the backscattering spectrum remains relatively consistent for the different incident energies. However, for larger incident angles, an increase in counts towards higher energy values for the backscattered electrons is observed. This indicates that, for higher incident angles, backscattered electrons lose less energy in the target detector. This is consistent with the observations of the backscattering tail in the target detector. Furthermore, it is observed that high-energy backscattering electrons are predominantly directed towards large

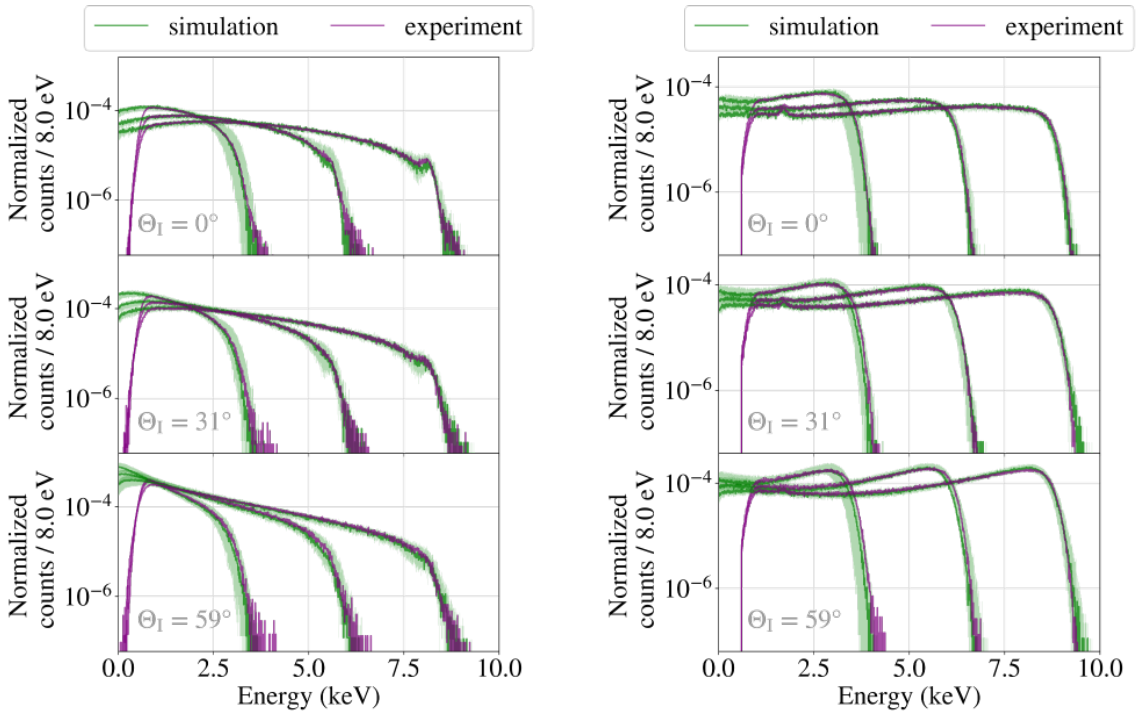

(a) Target detector

(b) Backscattering detector

Figure 5: Comparison of coincidence energy spectra. The spectra for coincidence events occurring in the target detector (figure 5a) and the backscattering detector (figure 5b) are depicted. Each panel shows the spectra for the three different settings of the initial electron energies at a given incident angle. The counts in the spectra are normalized to the total number of incoming electrons in the target detector. The light green band illustrates the uncertainty introduced in the simulation due to geometrical uncertainties in the experiment and uncertainties of the fitted transition layer parameters.

azimuthal backscattering angles. This phenomenon becomes more pronounced at larger incident angles.

The experimental and simulated spectra are in good agreement within the total uncertainty. However, slight discrepancies between the simulation and the experiment can be observed at the silicon escape peak, which is more prominent in the experimental data. This peak can be observed at 1.74 keV below the initial electron energy in the spectrum of the target detector. The corresponding photon peak in the backscattering detector is hence positioned at 1.74 keV. Furthermore, as the transition layer at the entrance window becomes more influential, the mismatch between the simulation and the experiment becomes more pronounced, particularly in the spectral decline at high energies. One possible explanation for this mismatch could be energy losses due to charge sharing. Even though the time stamps are utilized to identify charge sharing in the target detector, this identification method is limited due to the energy threshold of the data acquisition system. This problem could be mitigated in future measurements by reducing the electron beam size below the size of a singular pixel such that the charge sharing effects at the pixel border become neglectable.

To account for geometric uncertainties in the experiment and inaccuracies in the transition layer parameters used for the simulation, multiple simulations have been performed. Here, the values for the geometric positioning of the backscattering detector relative to the target detector in three dimensions, the incident and take-off angle, and the transition layer parameters are randomized from a flat distribution of values within the respective uncertainties of each parameter. The uncertainties associated with the geometric parameters are estimated based on the spatial and angular precision achievable within the experimental setup amounting to about 3 mm in position and 3° in angle. Uncertainties associated with the transition layer parameters are given in section 3. The resulting variation between the simulations is illustrated as an error band in figure 5. This method of using multiple simulations with randomized input parameters provides a rough estimation of the total error and the variability of the energy spectra given the uncertainties on various input parameters, which is sufficient for the work presented here.

4.2 Backscattering coefficients

The backscattering coefficient is a fundamental parameter quantifying the relation between incoming and backscattered electrons. It is calculated by taking the ratio of electrons detected in the backscattering detector to those measured in the target detector. To account for the detection efficiency, this ratio is appropriately scaled. The detection efficiency depends on the spatial coverage and positioning of the backscattering detector, as well as on the charge collection efficiency in combination with the detector energy threshold. The detection efficiency is obtained from simulations, where the ratio of generated and backscattered electrons to the experimentally measurable electrons can be determined. Furthermore, the number of detected incoming electrons in the target detector is corrected by the number of identified pileup and charge sharing events for the experimental data.

The backscattering coefficient depends on energy and angle, as depicted in figure 6. Specifically, there is a significant increase as the incident angle becomes larger. The backscattering coefficient more than doubles, comparing an incident angle of 59° with the minimal angle of 0°.

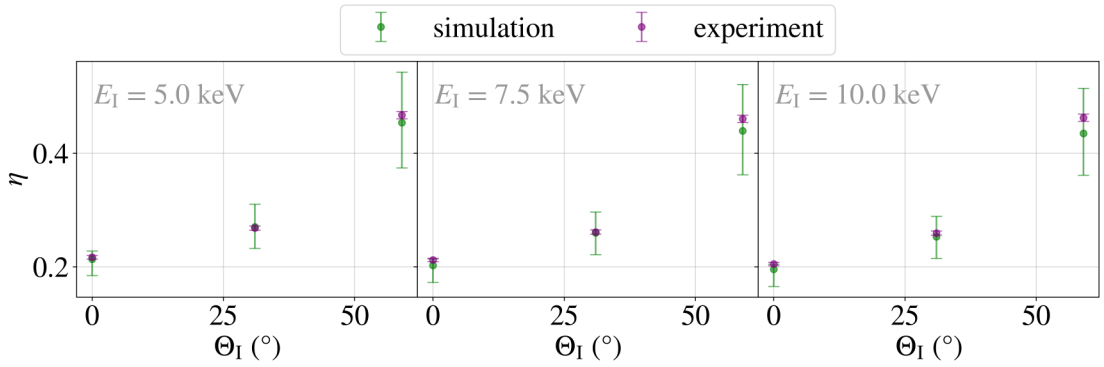

Figure 6: Comparison of backscattering coefficients. In each panel, the ratio of electrons detected in the backscattering detector to the electrons measured in the target detector is shown as a function of the incident angle at different initial electron energies. The backscattering coefficients are corrected for the backscattering detection efficiency.

Furthermore, a slight decrease of about 1 % in the backscattering coefficient is observed with increasing initial electron energy. The backscattering coefficients obtained from the experiment and the simulation are in good agreement regarding the backscattering coefficient within the uncertainties. Additionally, an agreement with literature values was found, which provides confidence in the reliability of the experimental and simulated measurements. For example, a backscattering coefficient of about 20.5 % for an initial electron energy of 10 keV and an incident angle of 0° is evaluated. This is in good agreement with literature values of around 17 – 21 % for silicon materials [26–29].

The errors for the simulation on the coefficients are again roughly estimated by considering the minimum and maximum values from a set of 10 simulations with randomly varied initial geometry and transition layer parameters conducted for each initial energy and incident angle configuration. For the experiment, a maximal uncertainty of 1 % each for the influence of pileup and charge sharing on the amount of measured incoming electrons is assumed.

5 Conclusions and outlook

For the investigation of the effect of electron backscattering on silicon drift detectors, an experimental test setup was designed and implemented. It consists of a heated tantalum wire as an electron source and two TRISTAN silicon drift detector devices to detect incoming and backscattered electrons. It was possible to explore the relationships between the energy and angle of incoming and backscattered electrons. Through a coincidence analysis, the contribution of backscattered electrons in the total energy spectrum of the target detector could be extracted. In a second step, GEANT4 simulations were used to model the detector response.

The experimental and simulation results show a good agreement within the uncertainties considered. Furthermore, the obtained backscattering coefficients, which quantify the ratio of backscattered to incoming electrons, align well with values reported in literature. It is worth noting that the accuracy of the transition layer modeling and the precision in geometric factors significantly impact the results. Improving the geometric accuracy of the experimental setup has a high potential to reduce the total uncertainty of the energy spectra and the backscattering coefficients. Furthermore, a more thorough investigation of the transition layer model combined with the inclusion of precise modeling of the data acquisition system should be performed to reach a higher agreement between simulation and experiment. In this respect, reducing the electron beam size to the diameter of a single pixel will also help mitigate spectral mismatches due to charge sharing in the target detector. Furthermore, measurements at very low electron rates can reduce the effect of pileup and mitigate the need for its rate-dependent modelling.

In summary, this study has introduced a method to measure the backscattering properties specific to the TRISTAN detector. We have validated the suitability of the GEANT4 simulation toolkit for backscattering investigations of silicon detectors. As a result, this work provides a foundation for an experimentally validated model of backscattering, vital for sensitivity studies and the forthcoming analysis of tritium spectra measured with the TRISTAN detector.

Acknowledgments

We acknowledge the support of Ministry for Education and Research BMBF (05A20PX3), Max Planck Research Group (MaxPlanck@TUM), Istituto Nazionale di Fisica Nucleare (INFN), Deutsche Forschungsgemeinschaft DFG Graduate School grant no. SFB-1258, and Excellence Cluster ORIGINS in Germany. This project has received funding from the European Research Council (ERC) under the European Union Horizon 2020 research and innovation programme (grant agreement no. 852845).

References

[1] K.N. Abazajian *et al.*, *Light Sterile Neutrinos: A White Paper*, 1204.5379.

[2] R. Adhikari *et al.*, *A White Paper on keV Sterile Neutrino Dark Matter*, *JCAP* **2017** (2017) 025.

[3] V. Domcke *et al.*, *MeV-scale seesaw and leptogenesis*, *JHEP* **2021** (2021) 200.

[4] R.N. Mohapatra *et al.*, *Theory of Neutrinos: A White Paper*, *Rep. Prog. Phys.* **70** (2007) 1757.

[5] A. Boyarsky, O. Ruchayskiy and D. Iakubovskyi, *A lower bound on the mass of dark matter particles*, *JCAP* **2009** (2009) 005.

[6] V.K. Narayanan, D.N. Spergel, R. Davé and C. Ma, *Constraints on the Mass of Warm Dark Matter Particles and the Shape of the Linear Power Spectrum from the Lyα Forest*, *ApJ* **543** (2000) L103.

[7] U. Seljak, A. Makarov, P. McDonald and H. Trac, *Can Sterile Neutrinos Be the Dark Matter?*, *Phys. Rev. Lett.* **97** (2006) 191303.

[8] B.W. Lee and R.E. Shrock, *Natural suppression of symmetry violation in gauge theories: Muon- and electron-lepton-number nonconservation*, *Phys. Rev. D* **16** (1977) 1444.

[9] A. Boyarsky, D. Iakubovskyi, O. Ruchayskiy and V. Savchenko, *Constraints on decaying dark matter from XMM-Newton observations of M31*, *Mon. Not. R. Astron. Soc.* **387** (2008) 1361.

[10] C.R. Watson, Z. Li and N.K. Polley, *Constraining sterile neutrino warm dark matter with Chandra observations of the Andromeda galaxy*, *J. Cosmol. Astropart. Phys.* **2012** (2012) 018.

[11] P. Pal and L. Wolfenstein, *Radiative decays of massive neutrinos*, *Phys. Rev. D* **25** (1982) 766.

[12] R.E. Shrock, *New tests for and bounds on neutrino masses and lepton mixing*, *Phys. Lett. B* **96** (1980) 159.

[13] S. Mertens *et al.*, *A novel detector system for KATRIN to search for keV-scale sterile neutrinos*, *J. Phys. G: Nucl. Part. Phys.* **46** (2019) 065203.

[14] KATRIN collaboration, *The design, construction, and commissioning of the KATRIN experiment*, *JINST* **16** (2021) T08015.

[15] S. Mertens, T. Brunst, M. Korzeczek, M. Lebert, D. Siegmann *et al.*, *Characterization of silicon drift detectors with electrons for the TRISTAN project*, *J. Phys. G: Nucl. Part. Phys.* **48** (2021) 015008.

[16] J.N. Abdurashitov *et al.*, *First measurements in search for keV sterile neutrino in tritium beta-decay in the Troitsk nu-mass experiment*, *JETP Lett.* **105** (2017) 753.

[17] E. Holzschuh *et al.*, *Search for heavy neutrinos in the β-spectrum of* ^{63}Ni, *Phys. Lett. B* **451** (1999) 247.

[18] E. Holzschuh, L. Palermo, H. Stüssi and P. Wenk, *The β-spectrum of* ^{35}S *and search for the admixture of heavy neutrinos*, *Phys. Lett. B* **482** (2000) 1.

[19] M. Gugiatti *et al.*, *Characterisation of a silicon drift detector for high-resolution electron spectroscopy*, *Nucl. Instrum. A* **979** (2020) 164474.

[20] D. Siegmann, F. Edzards, C. Bruch *et al.*, *Development of a Silicon Drift Detector Array to Search for keV-scale Sterile Neutrinos with the KATRIN Experiment*, *J. Phys. G: Nucl. Part. Phys.* (2024) .

[21] K. Urban *et al.*, *A thermionic electron gun to characterize silicon drift detectors with electrons*, 2404.01777.

[22] C. Forstner, *Characterization of a TRISTAN Silicon Drift Detector Array with a Laser System*, master's thesis, Technical University of Munich, 2023, https://www.ph.nat.tum.de/neutrinos/theses/.

[23] GEANT4 collaboration, *Geant4 - A simulation toolkit, Guide for Physics Lists*, https://geant4-userdoc.web.cern.ch/UsersGuides/PhysicsListGuide/html/index.html.

[24] D. Siegmann, *Investigation of the Detector Response to Electrons of the TRISTAN Prototype Detectors*, master's thesis, Technical University of Munich, 2019, https://www.ph.nat.tum.de/neutrinos/theses/.

[25] A. Nava, M. Biassoni, S. Pozzi, M. Gugiatti *et al.*, *A Geant4-based model for the TRISTAN detector*, *J. Phys.: Conf. Ser.* **2156** (2021) 012177.

[26] H. Drescher, R. Reimer and H. Seidel, *Rückstreukoeffizient und Sekundärelektronen-Ausbeute von 10-100 keV-Elektronen und Beziehungen zur Raster-Elektronen-Mikroskopie*, *Zeitschrift für Angewandte Physik* **29** (1970) 331.

[27] D. Joy, *A database on electron-solid interactions*, *Scanning* **17** (1995) 270.

[28] F. Akbari, *A comprehensive open-access database of electron backscattering coefficients for energies ranging from 0.1 keV to 15 MeV*, *MEDICAL PHYSICS* **50** (2023) 5920.

[29] P. Renschler, *KESS - A new Monte Carlo simulation code for low-energy electron interactions in silicon detectors*, ph.d. thesis, Karlsruhe Institute of Technology, 2011, https://publikationen.bibliothek.kit.edu/1000024959.